ISSN 1068-1620, Russian Journal of Bioorganic Chemistry, 2025, Vol. 51, No. 3, pp. 1346–1364. © Pleiades Publishing, Ltd., 2025.

Assessment of Cytotoxic Potentials of Isoindole-Derived Compounds with Epoxy Alcohol Functionalities on Different Cancer Cell Lines and Molecular Docking Analysis

Egehan Yetişkin[a], Özlem Gündoğdu[b], Derya Mete[a], Nurhan H. Kishali[c], Yunus Kara[c,*], and Gülşah Şanlı-Mohamed[a,]**

[a] *Department of Chemistry, Faculty of Sciences, İzmir Institute of Technology, Izmir, 35430 Turkey*
[b] *Vocational School of Kaman, Ahi Evran University, Kırşehir, 40100 Turkey*
[c] *Department of Chemistry, Faculty of Sciences, Ataturk University, Erzurum, 25240 Turkey*
**e-mail: yukara@atauni.edu.tr; **e-mail: gulsahsanli@iyte.edu.tr*

Received December 12, 2024; revised December 22, 2024; accepted December 24, 2024

Abstract—Objective: Isoindoline and epoxycyclohexane derivatives are known to exert beneficial effects on various inflammatory pathologies, including cancer. This study uniquely evaluates the cytotoxic potential of four synthesized isoindoline derivatives against five different cancer cell lines. **Methods:** Cancer cell lines were treated with varying concentrations of each derivative and incubated for 24, 48, and 72 h. Cytotoxicity was assessed via cell growth inhibition assays and cell membrane damage tests. Additionally, molecular docking studies were conducted to examine the interaction of the compounds with key cancer-related proteins: human tankyrase 1, c-MET, estrogen receptor alpha, androgen receptor, and EGFR. **Results and Discussion:** The epoxy alcohol derivatives demonstrated a dose-dependent cytotoxic effect, inhibited cell proliferation, and induced membrane damage in adenocarcinoma cell lines. Apoptosis rates and *in vitro* wound healing assays further supported their antiproliferative potential. **Conclusions:** These findings suggest that epoxy isoindole derivatives may serve as promising anticancer agents for the treatment of cervical, lung, prostate, and breast cancers due to their cytotoxic and antiproliferative activities. Molecular docking results corroborated their potential mechanism of action.

Keywords: isoindole-1,3-dione, epoxy alcohol, cytotoxicity, cancer cell lines, cell cycle analysis, molecular docking

DOI: 10.1134/S1068162024606657

INTRODUCTION

Polyoxygenated epoxy-cyclohexane derivatives are frequently found in the structure of various natural products [1, 2]. These compounds exhibit a range of noteworthy biological activities, including antitumor, antibacterial, and antifungal effects [2]. For instance, Eupenoxide (**I**) (Scheme 1), a cyclohexanoid metabolite isolated from a fungus of the *Eupenicillium species*, was stereospecifically synthesized by Duke and Rickards and is known for its antibiotic properties [3].

Additionally, compounds such as crotepoxide (**III**), senepoxide (**IV**), and pipoxide (**V**) (Scheme 2), which are chonduritol derivatives, are recognized as plant-derived tumor inhibitors with demonstrated antileukemic activity [4, 5].

More recently, certain isoindole derivatives have been identified to possess anticancer properties (Scheme 3). For example, we previously examined the cytotoxic effects of epoxy alcohol (**VIa**) against HT-29 colon adenocarcinoma cells using the MTT assay, revealing a dose-dependent cytotoxic effect [6].

Furthermore, the biological activity of derivatives such as diacetoxy (**VII**) and chloro/acetoxy (**VIII**) (Scheme 3) was investigated against HeLa cell lines [7, 8].

Experimental results indicate that the antiproliferative activity of these compounds is influenced by the nature of the substituent attached to the nitrogen atom of the

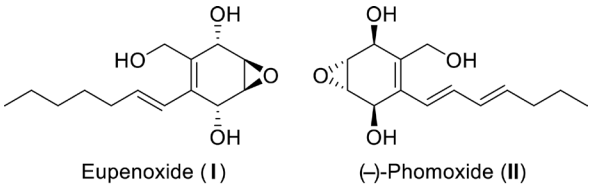

Scheme 1. Structures of eupenoxide (**I**) and phomoxide (**II**).

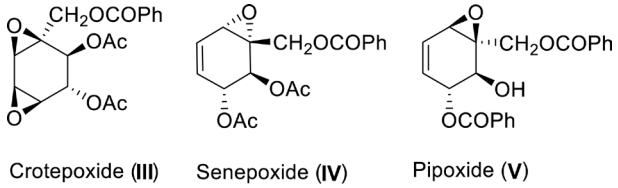

Scheme 2. Structures of crotepoxide (**III**), senepoxide (**IV**), and pipoxide (**V**).

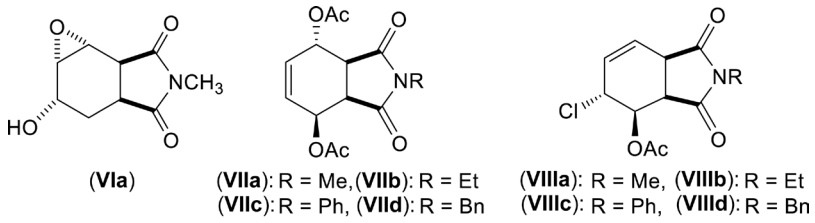

Scheme 3. Structures of some isoindole derivatives.

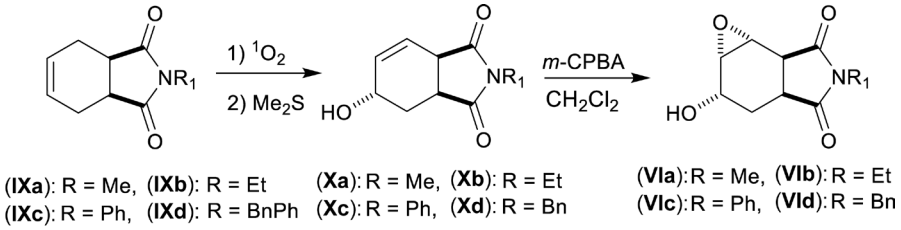

Scheme 4. Synthesis of epoxy alcohols derivatives (**VIa–VId**).

imide ring. Specifically, derivatives with ethyl, methyl, benzyl, and phenyl groups exhibited varying degrees of cytotoxic effects.

In light of the notable biological activity observed in both cyclohexane epoxides and isoindole derivatives, we aimed to synthesize hybrid molecules incorporating both structural motifs. The current study focuses on the synthesis and biological evaluation of epoxy alcohol derivatives (**VIa–VId**), each bearing a different nitrogen substituent, for their antiproliferative activity against five human cancer cell lines: HeLa (cervical), A549 (lung), PC3 (prostate), Caco-2 (colon), and MCF-7 (breast). Herein, we report the *in vitro* cytotoxicity of these novel isoindole-epoxy alcohol derivatives.

RESULTS AND DISCUSSION

In our previous work, we reported a straightforward five-step synthesis of epoxy alcohol compounds starting from 3-sulpholene [6, 9, 10]. The synthetic route is summarized in Scheme 4. Initially, singlet oxygen underwent an ene reaction with the bicyclic imides (**IXa–IXd**), forming a peroxide intermediate that was subsequently reduced to the corresponding alcohol. The resulting allyl alcohols (**Xa–Xd**) were then subjected to epoxidation using a peracid to yield the epoxy alcohols

(**VIa–VId**). These final products were characterized by ^{1}H, ^{13}C NMR, and mass spectrometry. Following structural confirmation, the anticancer activities of epoxy alcohol derivatives (**VIa–VId**) were evaluated.

Biological Evaluation

The cytotoxic effects of the epoxy alcohol derivatives (**VIa–VId**) were evaluated by measuring cell viability using the MTT assay. Figure 1 illustrates the viability of HeLa, A549, PC-3, Caco-2, and MCF-7 cell lines following exposure to compounds (**VIa–VId**) at varying concentrations (1000, 500, 250, 100, 50, and 25 μM) for 24, 48, and 72 h.

The results demonstrated that all tested compounds exhibited significant, dose- and time-dependent cytotoxicity across the investigated cell lines. A clear correlation was observed between increasing compound concentration and reduced cell viability. Additionally, longer incubation times enhanced the inhibitory effects. Based on overall response patterns, 48 h was identified as the optimal exposure period for compounds (**VIa–VId**) across all cell lines.

In A549 cells, compounds (**VIa–VId**) induced a marked dose-dependent cytotoxic effect after 48 h, with compound (**VId**) showing the lowest IC_{50} value, indicating the highest potency (Table 1).

In the HeLa cell line, cell viability significantly decreased at concentrations ≥ 250 μM, particularly after 48 and 72 h of treatment. For instance, compound (**VIb**) reduced viability from 64% after 24 h to 9% after 72 h, while compound (**VIc**) displayed consistent cytotoxicity across all exposure times at lower concentrations. However, at higher doses (1000–250 μM), viability dropped sharply to around 8%. Once again, compound (**VId**) was the most effective in reducing HeLa cell viability after 48 h.

Comparable results were observed in the PC-3 cell line. Compound (**VId**) exhibited the highest potency, significantly decreasing cell viability even at the lowest concentration tested (25 μM), from 75 to 53% after 48 h.

In the MCF-7 cell line, the effects of the test compounds on cell viability were primarily time-dependent. However, for compounds (**VIb**) and (**VIc**), the incubation period had minimal influence on the overall cytotoxic effect (Fig. 1). With respect to dose dependency, compound (**VId**) showed a marked reduction in viability, decreasing to less than 37% at 250 μM after 72 h of exposure.

In Caco-2 cells, compound (**VId**) emerged as the most effective agent. Although cell viability remained relatively stable across time points, it decreased significantly to 19% at concentrations of 50 μM and higher after 72 h (Fig. 1).

To investigate the mechanism of cytotoxicity, the apoptotic effects of compounds (**VIa–VId**) were assessed in A549, HeLa, PC-3, MCF-7, and Caco-2 cell lines using the FITC annexin V apoptosis detection kit combined with propidium iodide (PI). Cells were treated with each compound at their respective IC_{50} concentrations and incubated for 48 h. Apoptotic profiles were analyzed *via* flow cytometry and compared to untreated control groups.

In A549 cells, treatment with compound (**VId**) led to the highest rate of late apoptosis, while necrosis levels were comparable across all tested compounds. This finding aligns with the results from the MTT assay, indicating the superior cytotoxicity of compound (**VId**).

In HeLa cells, all compounds significantly increased both early and late apoptosis compared to controls. Among them, compound (**VId**) induced the highest early apoptosis (8%), while compound (**VIc**) exhibited the highest late apoptosis (19%).

For PC-3 cells, all four compounds elicited apoptosis with similar early apoptosis rates. Notably, compound (**VIa**) showed the most pronounced late apoptosis, reaching 15% (Fig. 2).

In MCF-7 cells, the compounds did not cause significant necrosis but did result in elevated apoptosis, thereby decreasing the percentage of viable cells. In the Caco-2 cell line, compound (**VId**) was once again the most effective, reducing the proportion of viable cells to 21%, consistent with its strong cytotoxic effect observed in the MTT assay (Fig. 1).

Taken together, apoptosis analysis following 48-h incubation confirms that compound (**VId**) exhibits superior apoptotic and cytotoxic activity compared to the other tested derivatives.

Fig. 1. The cell viability of A549, PC-3, HeLa, Caco-2, and MCF-7 cell lines exposed to (a) **(VIa)**, (b) **(VIb)**, (c) **(VIc)**, and (d) **(VId)** drugs at different concentrations (1000–500–250–100–50–25 μM) at 24, 48, and 72 h, respectively.

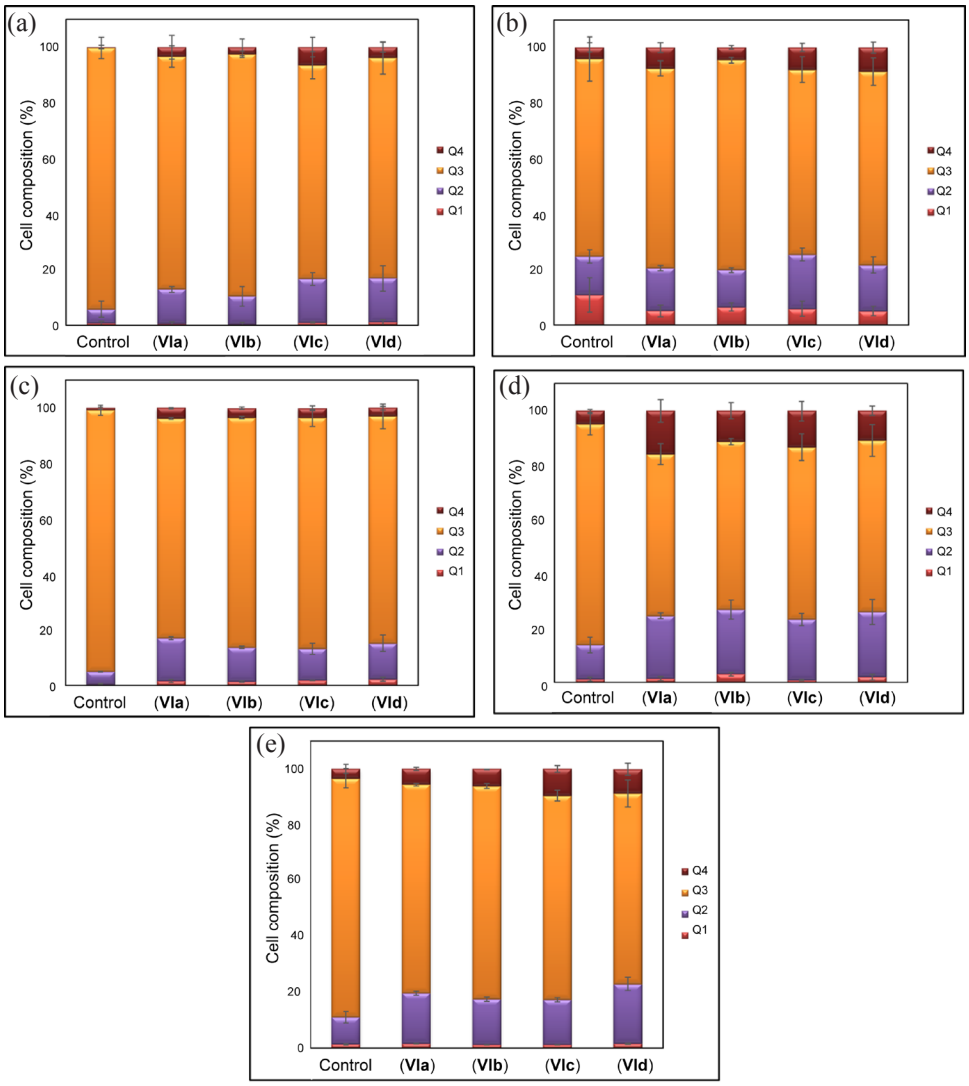

Fig. 2. The apoptotic effects of (**VIa–VId**) compounds on A549 (a), HeLa (b), PC-3 (c), MCF-7 (d), and Caco-2 (e) cells, each drug were applied at their own IC_{50} concentrations at 48-h incubation time.

Table 1. IC_{50} values of the (**VIa–VId**) compounds at 48-h incubation time were calculated for HeLa, A549, PC-3, Caco-2, and MCF-7 cell lines

Compound (IC_{50}, μM)	Cell lines				
	HeLa	A549	PC3	CaCo-2	MCF-7
(VIa)	148.7 ± 86.5 $R^2 = 0.91$	307.8 ± 72.4 $R^2 = 0.90$	338.8 ± 80.9 $R^2 = 0.92$	295.3 ± 96.6 $R^2 = 0.81$	263.3 ± 48.9 $R^2 = 0.89$
(VIb)	155.2 ± 26.7 $R^2 = 0.96$	161.0 ± 45.8 $R^2 = 0.95$	242.0 ± 48.9 $R^2 = 0.92$	136.3 ± 28.7 $R^2 = 0.94$	274.6 ± 51.4 $R^2 = 0.91$
(VIc)	179.3 ± 69.0 $R^2 = 0.96$	192.3 ± 62.7 $R^2 = 0.90$	204.7 ± 33.4 $R^2 = 0.99$	208.5 ± 42.0 $R^2 = 0.93$	302.1 ± 40.5 $R^2 = 0.97$
(VId)	99.81 ± 15.1 $R^2 = 0.99$	69.65 ± 12.8 $R^2 = 0.99$	110.5 ±37.2 $R^2 = 0.97$	77.41 ± 22.3 $R^2 = 0.95$	225.1 ± 20.1 $R^2 = 0.94$

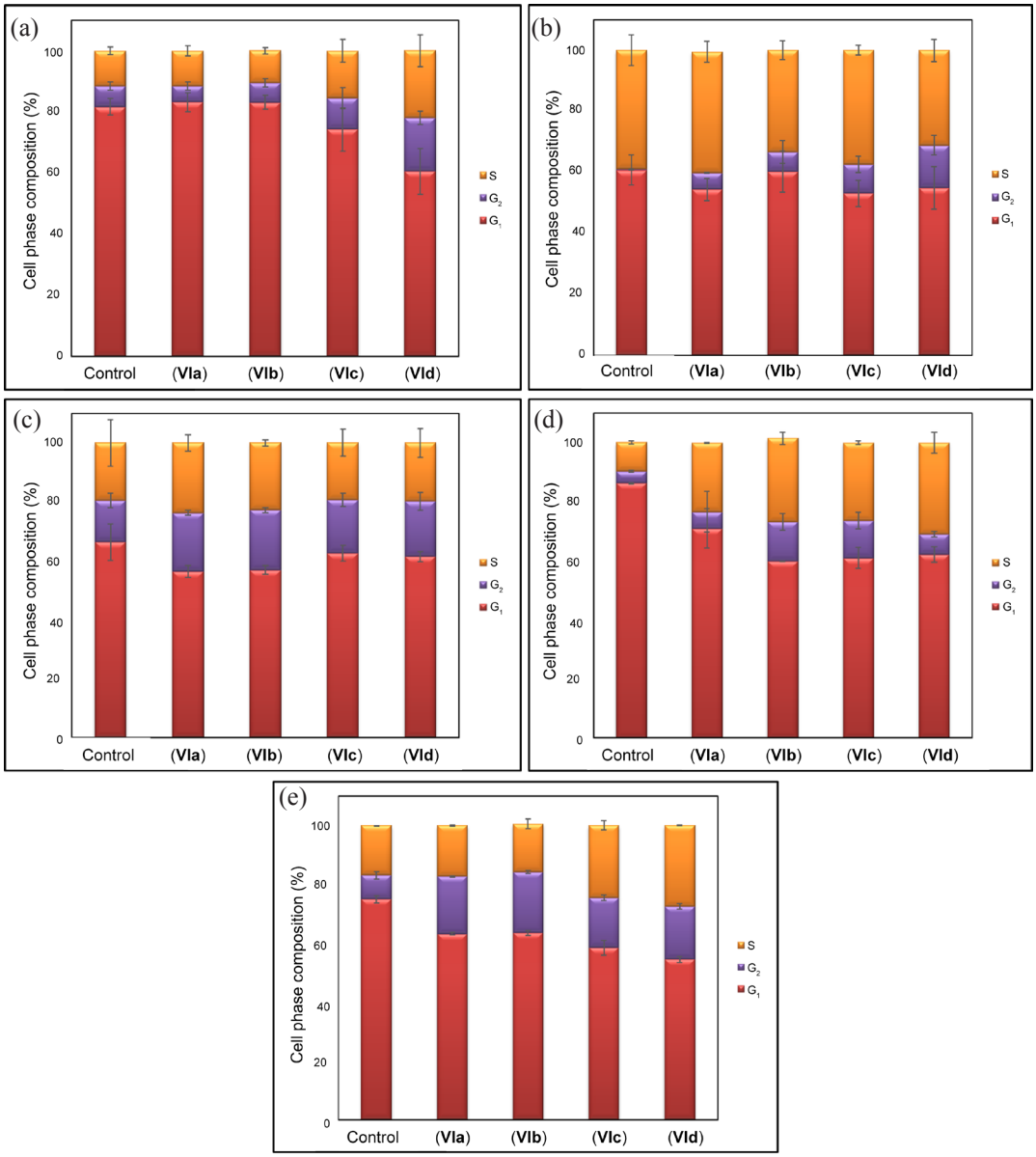

Fig. 3. The cell cyle of (**VIa–VId**) compounds on A549 (a), HeLa (b), PC-3 (c), MCF-7 (d), and Caco-2 (e) cells, each drug were applied at their own IC_{50} concentrations at 48-h incubation time.

The effects of compounds (**VIa–VId**) on the cell cycle progression were evaluated in A549, HeLa, PC-3, MCF-7, and Caco-2 cell lines. Each compound was applied at its respective IC_{50} concentration for 48 h. Flow cytometric analysis of cell cycle distribution (G_1, S, and G_2/M phases) was performed following propidium iodide (PI) staining, with 10000 events recorded per sample (Fig. 3). Untreated cells were used as the negative control.

In A549 cells, compounds (**VIa**) and (**VIb**) produced similar cell cycle profiles, whereas (**VIc**) and (**VId**) caused a noticeable G_2/M phase arrest. Notably, compound (**VId**) increased the G_2/M population by 17%, suggesting inhibition of DNA replication and cell division.

In HeLa cells, all compounds induced varying levels of G_2/M phase arrest, with G_2/M phase populations reaching 5, 6, 9, and 14% for compounds (**VIa–VId**), respectively.

In the PC-3 cell line, compounds (**VIa**) and (**VIb**) led to a reduction in the G_1 phase population, whereas (**VIc**) and (**VId**) caused a corresponding increase in the G_2/M phase, indicating a shift in the cell cycle checkpoint control.

In MCF-7 cells, treatment with compounds (**VIb**) and (**VIc**) significantly elevated the G_2/M phase population by 13 and 12%, respectively, thereby suppressing cell proliferation through inhibition of mitosis.

In Caco-2 cells, all tested compounds notably increased the S phase population, indicating DNA synthesis activity. Additionally, compound (**VIb**) led to a marked elevation in the G_2/M phase up to 20%, suggesting a dual blockade at both S and G_2/M checkpoints.

For comparison, Sharma et al. investigated 34 newly synthesized diindolylmethane derivatives in HeLa, A549, and MCF-7 cell lines. Their findings revealed that a specific indole derivative caused G_1 phase arrest in HeLa cells, while MCF-7 cells were comparatively less sensitive than A549 and HeLa cells [17].

These results underline the phase-specific and cell line-specific effects of epoxy alcohols (**VIa–VId**) and support their potential as selective anticancer agents targeting cell cycle progression in tumor cells.

The *in vitro* wound healing assay (scratch assay) was performed to evaluate the anti-migratory effects of compounds (**VIa–VId**) on various cancer cell lines. This method involves creating a uniform scratch (artificial wound) in a confluent monolayer of cells and observing the ability of cells at the wound edge to migrate and close the gap. The A549, HeLa, PC3, Caco-2, and MCF-7 cell lines were treated with the respective IC_{50} concentrations of each compound, and wound closure was monitored at 0, 24, and 48 h using an inverted phase-contrast microscope. Images were analyzed to quantify the percentage of wound closure (Figs. 4–5).

In A549 cells, compound (**VIb**) exhibited the strongest inhibition of cell migration, resulting in the lowest gap closure after 48 h. Compounds (**VIc**) and (**VId**) also significantly reduced migration, with closure rates of 15 and 14%, respectively, which correlated with increased cell death observed microscopically.

In the HeLa cell line, compound (**VIc**) demonstrated the highest anti-migratory activity, followed by (**VId**), with respective gap closure rates of 21% and slightly higher for (**VId**).

For PC3 cells, compound (**VId**) again showed the most pronounced inhibition of migration (9% closure), followed by (**VIc**) (12%), (**VIb**) (17%), and (**VIa**) (22%). These results were consistent with the cytotoxic profiles of the compounds observed in earlier assays (Fig. 4).

In MCF-7 cells, all compounds exhibited strong anti-migratory effects, with gap closure rates below 1% after 48 h. Microscopic evaluation also revealed substantial cell death, further contributing to the minimal migration observed.

In Caco-2 cells, compound (**VId**) displayed the lowest migration rate, with a gap closure of only 7%, again highlighting its potent anti-migratory and cytotoxic effects.

Overall, these findings confirm that compounds (**VIa–VId**), particularly (**VIc**) and (**VId**), significantly impair cell motility and migration in a cell line-dependent manner, underlining their potential as anti-metastatic agents (Figs. 4–5).

Molecular Modeling Studies

Molecular modeling is a powerful tool in the rational design of novel therapeutic agents and in elucidating the mechanisms underlying drug–protein interactions [18, 19]. In this study, molecular docking analyses were conducted to investigate the anticancer potential of isoindole-epoxyalcohol derivatives, specifically focusing on compounds (**VIb**) and (**VId**), which demonstrated the highest cytotoxic activity *in vitro* against A549, PC3, HeLa, MCF-7, and Caco-2 cell lines.

Docking simulations were performed to evaluate the ligand–protein binding interactions, aiming to understand

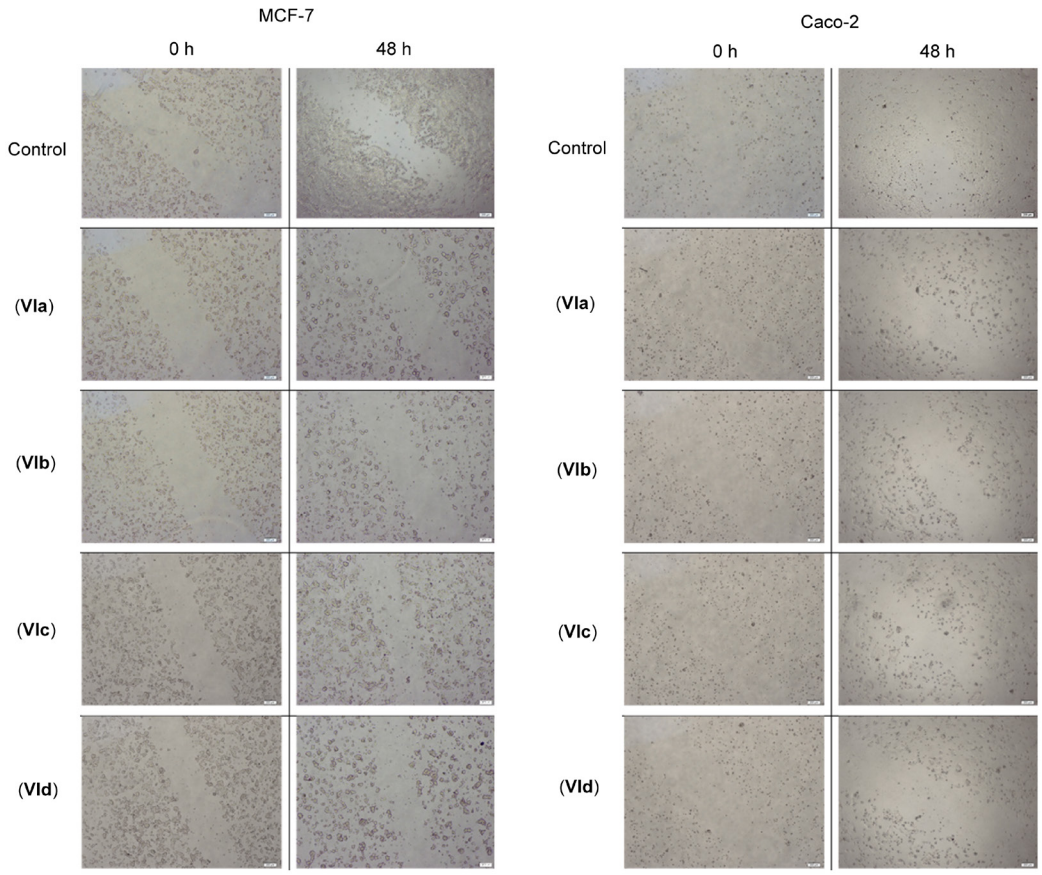

Fig. 4. Images of cell migration on MCF7 and Caco-2 monolayers in control and IC_{50} concentrations treated of (**VIa–VId**) at 0 h and 48 h incubation.

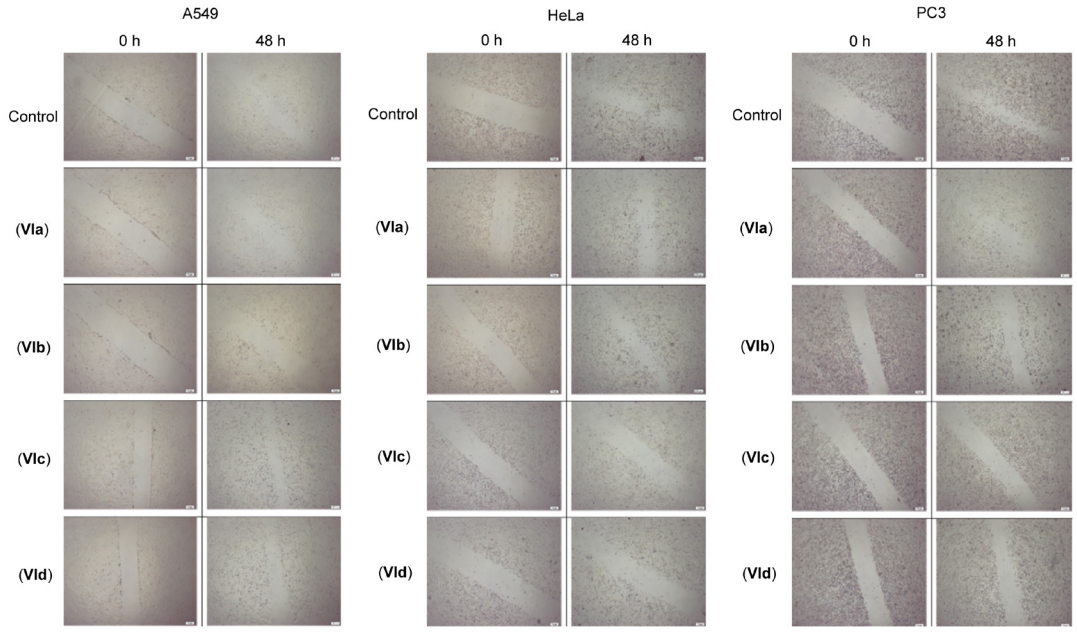

Fig. 5. The effect of compounds (**VIa–VId**) on cell migration by *in vitro* wound healing assay on A549, HeLa, and PC3 cell lines.

the underlying mechanisms of action and inhibition. The molecular interactions between the compounds and target proteins associated with cancer progression were assessed using validated docking protocols. The detailed 2D and 3D interaction profiles of compounds (**VIb**) and (**VId**) with their respective targets are illustrated in the supplementary information (Figs. S6 and S7).

The active binding sites of all selected cancer-related target proteins—including tankyrase 1 (PDB ID: 2ITO), estrogen receptor α (3ERT), androgen receptor (4GG5), c-MET kinase (2AX6), and EGFR tyrosine kinase (4W6E)—were defined for molecular docking. Key parameters such as binding site geometry, stability of ligand anchoring, and a variety of non-covalent interactions, including van der Waals forces, π–π stacking, hydrogen bonding, and hydrophobic/hydrophilic contacts, were taken into account to assess the binding affinity and interaction quality.

Compound (**VId**) (*N*-benzyl derivative) exhibited the most favorable docking results across all tested receptors. Specifically, its calculated binding energies were −6.50 kcal/mol for 2ITO, −7.78 kcal/mol for 3ERT, −7.12 kcal/mol for 4GG5, −8.98 kcal/mol for 2AX6, and −8.83 kcal/mol for 4W6E, indicating strong and stable interactions within each target protein's active site. These results suggest that compound (**VId**) has a broad-spectrum binding potential and a high affinity for multiple cancer-related receptors.

Detailed docking analyses, shown in Fig. 6, reveal that compound (**VId**) forms multiple hydrogen bonds with key amino acid residues at the catalytic sites of these targets. Notably, the carbonyl group of the phthalimide moiety in (**VId**) formed hydrogen bond interactions with the MET793 residue in both 2ITO and 2ITU, with bond lengths of 2.07 and 2.068 Å, respectively. These interactions play a crucial role in stabilizing the ligand–protein complexes and likely contribute to the compound's observed in vitro efficacy.

Taken together, the docking results are in strong agreement with the experimental cytotoxicity data and support the potential of epoxyisoindole derivatives, particularly compound (**VId**), as promising candidates for targeted anticancer therapy.

Docking into Epidermal Growth Factor Receptor (EGFR)

Epidermal growth factor receptor (EGFR), a member of the receptor tyrosine kinase (RTK) family, is a key cell signaling effector involved in cancer development [20]. The EGFR gene has been targeted for the treatment of various cancers, including pancreatic, non-small cell lung carcinoma (NSCLC), colorectal, and breast cancers [21]. Therefore, we investigated the interactions of the two most active compounds, (**VIb**) (*N*-Et) and (**VId**) (*N*-Bn), with EGFR using a molecular docking approach.

Binding energy values for compound (**VId**) (*N*-Bn) ranged from –6.77 to –8.40 kcal/mol, while for compound (**VIb**) (*N*-Et) these values ranged from –4.24 to –5.69 kcal/mol. Compound (**VId**) (*N*-Bn) demonstrated better binding affinity (lowest energy –8.40 kcal/mol) compared to (**VIb**) (*N*-Et) (–5.69 kcal/mol). The best binding energy of (**VId**) (*N*-Bn) corresponded to its superior anticancer effect.

In the interaction of (**VId**) (*N*-Bn) with EGFR, the hydroxyl group formed a conventional hydrogen bond with Met793 (4.83 Å), and three π-alkyl interactions were observed with Leu788 (6.53 Å), Ala743 (5.79 Å), and Lys745 (4.10 Å). Additionally, π-sulfur interaction was noted with Met766 (7.83 Å), and a π-cation interaction with Lys745 (4.10 Å). The phenyl group formed a π-sigma interaction with Thr790 (5.24 Å). Other interactions are detailed in Table 2 and Fig. 5. The EGFR structure was retrieved from the Protein Data Bank (PDB ID: 2ITO) (https://www.rcsb.org/).

Docking into Human Tankyrase 1 (PDB ID: 4W6E)

Colorectal cancer is the leading cause of cancer-related deaths worldwide. Several proteins, including protein kinase CK2α and human tankyrases (TNKS), have been reported to play antiapoptotic roles in cell proliferation and uncontrolled growth when overexpressed. Although many drugs have been developed targeting these proteins, their clinical application is limited due to high

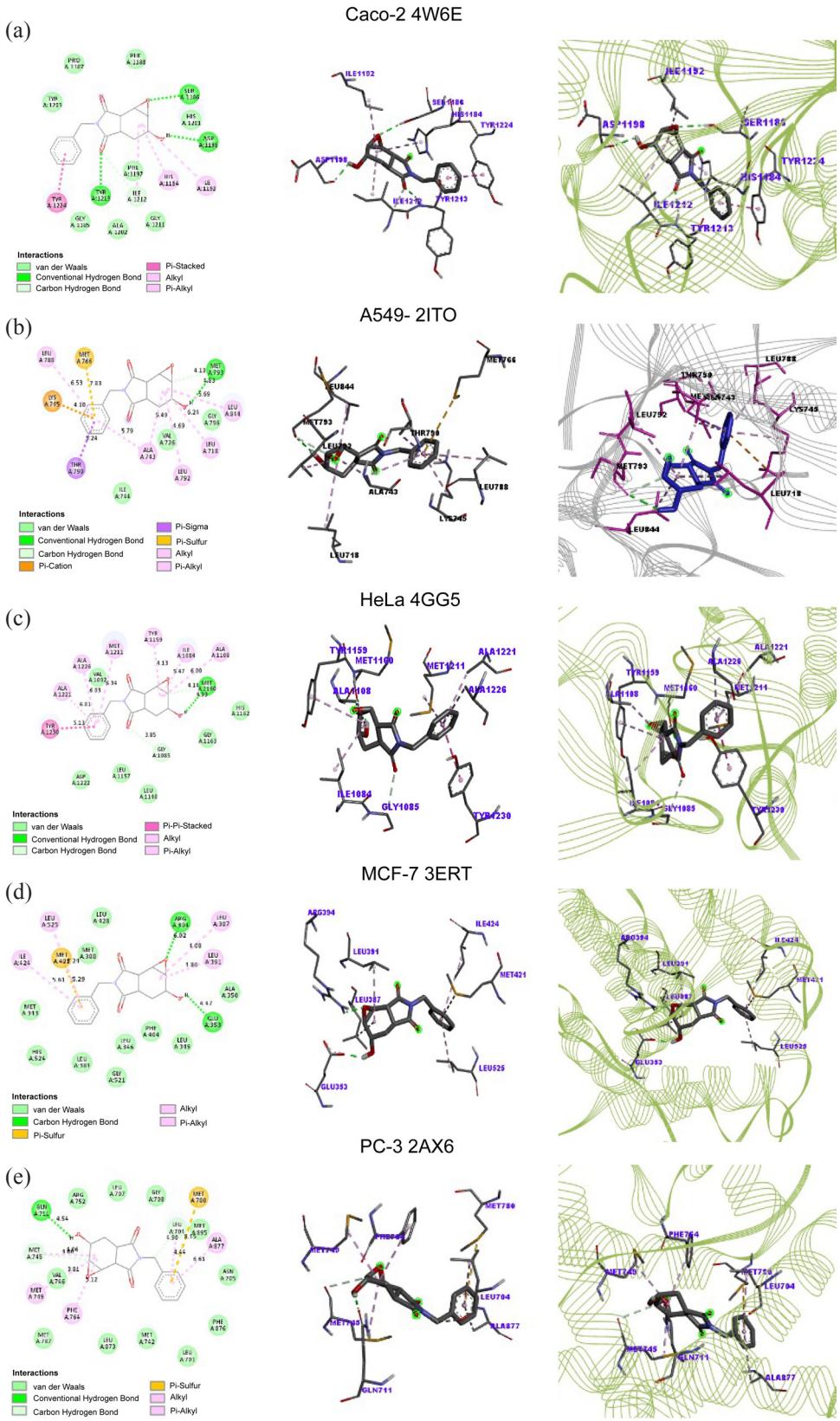

Fig. 6. 3D and 2D representation of binding interactions of (**VId**) (*N*-Bn) with (a) 4W6E, (b) 2ITO, (c) 4GG5, (d) 3ERT, and (e) 2AX6.

Table 2. Docking energy values with different interacting atoms and compound (**VId**) (*N*-Bn)

Protein	Residues and bond distance (Å)	Docking energy (kcal/mol)
PDB ID: 4W6E (CaCO-2)	HIS1184 (7.61), ILE1212 (6.47), ILE1192 (5.35), TYR1224 (5.01), ILE1212 (3.86), ASP1198 (3.42), SER1186 (5.04)	–8.83
PDB ID: 2ITO (A549)	MET766 (7.83), LYS745 (4.10), LEU844 (5.69), LEU718 (6.24), LEU792 (4.69), ALA743 (5.49), THR790 (5.24), ALA743 (5.79), LYS745 (4.10), LEU788 (6.53), MET793 (4.13), MET793 (4.83)	–6.50
PDB ID: 4GG5 (HELA)	ALA1221 (6.81), ALA1226 (6.03), Met121 (6.34), TYR1159 (4.13), ALA1108 (6.00), ILE1084 (5.47), TYR1230 (5.13), MET1160 (4.14), GLY1085 (3.85), MET1160 (4.93)	–7.12
PDB ID: 3ERT (MCF-7)	GLU353 (4.47), ARG394 (6.02), LEU387 (4.08), LEU391 (4.86), LEU525 (7.24), ILE424 (5.61), MET421 (5.29)	–7.78
PDB ID: 2AX6 (PC-3)	MET780 (8.45), PHE764 (5.12), LEU704 (4.44), ALA877 (6.61), MET745 (4.06), MET749 (3.81), LEU704 (4.90), MET745 (4.06), GLN711 (4.54)	–8.98

toxicity, side effects, and resistance to treatment [22]. Tankyrase 1 and tankyrase 2 are poly(ADP-ribose) polymerases involved in pathways critical for cancer cell growth [23, 24]. Recently, inhibition of tankyrases and/or protein kinase CK2α has emerged as a promising strategy in anticancer drug discovery [22].

Therefore, we investigated the interactions of the two most active compounds (**VIb** and **VId**) with human tankyrase 1 using molecular docking. The structure of human tankyrase 1 in complex with a native inhibitor was retrieved from the Protein Data Bank (PDB ID: 4W6E) (https://www.rcsb.org/). During preparation of the docking model, the cofactor (Zn^{2+} ion) and water molecules were removed.

Binding energy values for compound (**VId**) (*N*-Bn) ranged from –8.04 to –8.83 kcal/mol, while for compound (**VIb**) (*N*-Et) they ranged from –6.16 to –5.60 kcal/mol. Compound (**VId**) (*N*-Bn) showed better binding affinity (–8.83 kcal/mol) than (**VIb**) (*N*-Et) (–6.16 kcal/mol). The best binding energy for (**VId**) (*N*-Bn) corresponded to its superior anticancer activity.

In the interaction of (**VId**) (*N*-Bn) with human tankyrase 1, the hydroxyl and epoxide groups formed conventional hydrogen bonds with Asp1198 (3.42 Å) and Ser1186 (5.04 Å), respectively, and π-alkyl interactions with His1184 (7.61 Å). Additionally, a π-π stacked interaction was observed with Tyr1224 (5.01 Å). Other interactions are summarized in Table 2 and Fig. 6.

Docking into c-Met Hepatocyte Growth Factor Receptor (HGFR)

c-Met is a receptor tyrosine kinase with important signaling functions. It is also known as Met or hepatocyte growth factor receptor (HGFR). c-Met promotes cell proliferation, invasion, and survival in both normal and cancer cells. Tumor progression can be slowed by inhibiting c-Met activity [25, 26]. Several molecules have been identified as c-Met inhibitors; however, the discovery of effective c-Met inhibitors remains challenging due to their high cost and adverse side effects [25]. Therefore, we investigated the interactions of the two most active compounds, (**VIb**) (*N*-Et) and (**VId**)

(*N*-Bn), with tyrosine kinase c-Met using a molecular docking approach [27]. The c-Met structure in complex with its ligand was retrieved from the Protein Data Bank (PDB ID: 4GG5) (https://www.rcsb.org/).

Binding energy values for compound (**VId**) (*N*-Bn) ranged from –5.78 to –7.12 kcal/mol, while for compound (**VIb**) (*N*-Et), the values ranged from –4.81 to –5.38 kcal/mol. Compound (**VId**) (*N*-Bn) exhibited better binding affinity (–7.12 kcal/mol) compared to (**VIb**) (*N*-Et) (–5.38 kcal/mol). The lowest binding energy of (**VId**) (*N*-Bn) correlated with its superior anticancer activity.

In the interaction of (**VId**) (*N*-Bn) with the c-Met receptor, the hydroxyl group formed a conventional hydrogen bond with Met1160 (4.93 Å). π-Alkyl interactions were observed with Ala1221 (6.81 Å), Ala1226 (6.03 Å), Met121 (6.34 Å), and Tyr1159 (4.13 Å). Additionally, a π-π stacked interaction was noted with Tyr1230 (5.13 Å). Other interactions are detailed in Table 2 and Fig. 6.

Docking into Human Estrogen Receptor Alpha Ligand Binding Domain (PDB ID: 3ERT)

Estrogen receptor alpha (ERα) plays a crucial role in cell proliferation and is expressed in endometrial, breast, ovarian stromal cells, and the hypothalamus. The tamoxifen-bound ERα complex has been reported to inhibit estrogenic effects responsible for cancer cell proliferation [28–30]. Therefore, the crystal structure of the human estrogen receptor alpha ligand-binding domain in complex with 4-hydroxytamoxifen (PDB ID: 3ERT) was chosen for the docking study [29].

Herein, we investigated the interactions of compound (**VId**) (*N*-Bn) with the human estrogen receptor alpha ligand. Binding energy values for (**VId**) (*N*-Bn) ranged from –7.39 to –7.78 kcal/mol, while for (**VIb**) (*N*-Et) they ranged from –5.74 to –6.15 kcal/mol. Compound (**VId**) (*N*-Bn) demonstrated better binding affinity (–7.78 kcal/mol) compared to (**VIb**) (*N*-Et) (–6.15 kcal/mol). The lowest binding energy of (**VId**) (*N*-Bn) correlated with its superior anticancer effect.

In the interaction of (**VId**) (*N*-Bn) with the estrogen receptor alpha ligand (PDB ID: 3ERT), the hydroxyl and epoxide groups formed conventional hydrogen bonds with Glu353 (4.47 Å) and Arg394 (6.02 Å), respectively. π-Alkyl interactions were observed with Leu525 (7.24 Å) and Ile424 (5.61 Å). Additionally, a π-sulfur interaction was noted with Met421 (5.29 Å). Other interactions are summarized in Table 2 and Fig. 6.

Docking into Androgen Receptor Ligand Binding Domain (PDB ID: 2AX6)

Androgens and androgen receptors (AR) play crucial roles in diseases such as androgen insensitivity syndrome (AIS) and prostate cancer. The elucidation of the structures of the AR DNA-binding domain and ligand-binding domain has facilitated drug design for prostate cancer treatment [31, 32]. Therefore, the crystal structure of the androgen receptor ligand-binding domain T877A mutant in complex with hydroxyflutamide (PDB ID: 2AX6) was selected for this docking study [32, 33].

Herein, we investigated the interactions between compound (**VId**) (*N*-Bn, benzyl derivative) and the androgen receptor. Binding energy values for (**VId**) (*N*-Bn) ranged from –7.50 to –8.98 kcal/mol, whereas for compound (**VIb**) (*N*-Et) the values ranged from –4.61 to –5.95 kcal/mol. Compound (**VId**) (*N*-Bn) exhibited better binding affinity (–8.98 kcal/mol) than (**VIb**) (*N*-Et) (–5.95 kcal/mol). The lowest binding energy of (**VId**) (*N*-Bn) correlated with its superior anticancer activity.

In the interaction of (**VId**) (*N*-Bn) with the androgen receptor ligand-binding domain T877A mutant (in complex with hydroxyflutamide), the hydroxyl group formed a conventional hydrogen bond with Gln711 (4.54 Å). π-Alkyl interactions were observed with Phe764 (5.12 Å), Leu704 (4.44 Å), and Ala877 (6.61 Å). Additionally, a π-sulfur interaction occurred with Met780 (8.45 Å). Other interactions are summarized in Table 2 and Fig. 6.

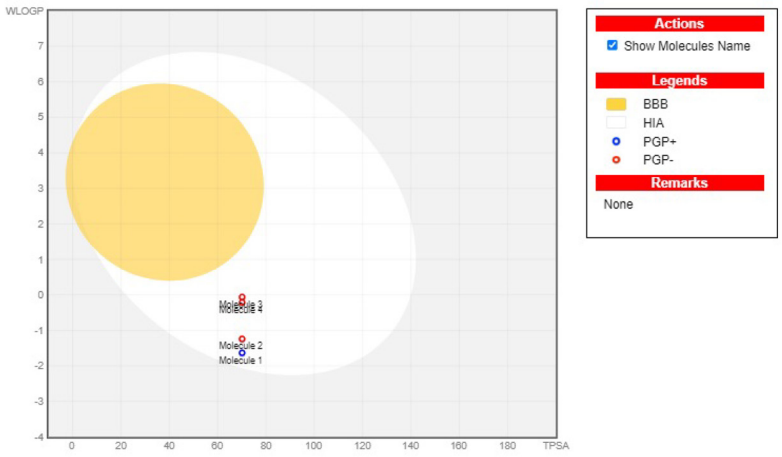

Fig. 7. BOILED-Egg model of (**VIa–VId**).

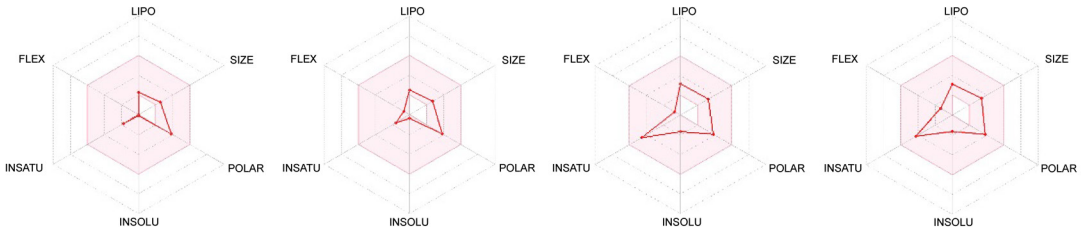

Fig. 8. Evaluation of drug properties of compounds by bioavailability radar.

ADME Analysis

The absorption, distribution, metabolism, and excretion (ADME) properties of the compounds were evaluated using SwissADME. The synthesized compounds complied with Lipinski's rule of five (Table 1). All compounds have molecular weights below 500 g/mol. Their log*P* values ranged from 1.47 to 2.05, satisfying the key criteria of Lipinski's rules [16, 34]. Pharmacokinetics evaluation results for compounds (**VIa–VId**) are presented in Table 3.

In silico ADMET predictions were performed to assess the synthesized compounds. Early prediction of pharmacokinetic properties helps prevent failure in clinical trials. Ideal drug candidates should be rapidly absorbed, evenly distributed, efficiently metabolized, and safely eliminated without adverse effects. As shown in Table 2, all compounds exhibit high gastrointestinal (GI) absorption. Estimated ADME properties are detailed in Table 4.

BOILED-Egg Model

The brain or intestinal estimated permeation method (BOILED-Egg) was used to predict gastrointestinal (GI) absorption and blood-brain barrier (BBB) permeability of small molecules [15]. In the BOILED-Egg diagram, the yellow region represents molecules with high BBB permeability, while the white region corresponds to molecules with high human intestinal absorption. All tested molecules fell within the white region, indicating a high likelihood of gastrointestinal absorption (Fig. 7).

The optimal range for key physicochemical properties—such as saturation, molecular size, lipophilicity, polarity, flexibility, and solubility—is depicted by the pink area on the bioavailability radar plots. Figure 8 illustrates the bioavailability radars for all compounds.

Table 3. Pharmacokinetics evaluation results of compounds

Compound	Formula	MW, g/mol (range ≤ 500)	TPSA, Å^2	No. rotatable bonds (range 1–10)	No. H-rotatable acceptors (range ≤ 10)	No. H-rotatable donors (range ≤ 5)	log$P_{o/w}$ (iLOGP) (range ≤ 5)	Lipinski violations
(**VIa**)	$C_9H_{11}NO_4$	197.19	70.14	0	4	1	1.47	0
(**VIb**)	$C_{10}H_{13}NO_4$	211.21	70.14	1	4	1	1.51	0
(**VIc**)	$C_{14}H_{13}NO_4$	259.26	70.14	1	4	1	1.76	0
(**VId**)	$C_{15}H_{15}NO_4$	273.28	70.14	2	4	1	2.05	0

Table 4. Pharmacokinetics properties of compounds calculated with the SwissADME program

Compound	GI absorption	BBB permeant	PGP substrate	CYP1A2 inhibitor	CYP2C19 inhibitor	CYP2C9 inhibitor	CYP2D6 inhibitor	CYP3A4 inhibitor	logK_p (skin permeation), cm/s
(**VIa**)	High	No	Yes	No	No	No	No	No	–8.57
(**VIb**)	High	No	No	No	No	No	No	No	–8.40
(**VIc**)	High	No	No	No	No	No	No	No	–7.85
(**VId**)	High	No	No	No	No	No	No	No	–7.98

EXPERIMENTAL

General chemistry. All reagents used in this study were obtained from commercial sources unless otherwise specified. All solvents were purified by distillation prior to use. Melting points were determined using a Gallenkamp melting point apparatus. Infrared (IR) spectra were recorded on a PerkinElmer Spectrum One FT-IR spectrometer. ^{1}H and ^{13}C NMR spectra were acquired on Varian and Bruker 400 MHz spectrometers. Elemental analysis was performed using a LECO CHNS-932 instrument.

General synthesis of epoxy alcohols (VIa–VId). Epoxy alcohols (**VIa–VId**) were synthesized *via* a five-step procedure starting from 3-sulfolene, following previously reported methodologies [6, 9, 10]. The chemical structures of the synthesized epoxy alcohols were confirmed through comprehensive spectral analyses, including ^{1}H, ^{13}C NMR, and mass spectrometry (MS).

Biological evaluation. Cell culture. HeLa (cervical), A549 (lung), PC3 (prostate), and MCF-7 (breast) cancer cell lines were obtained from the Biotechnology and Bioengineering Research Center at Izmir Institute of Technology. The Caco-2 (colon) cell line was provided by the Izmir International Biomedicine and Genome Institute. HeLa and MCF-7 cells were cultured in RPMI 1640 medium (Lonza), while PC3, Caco-2, and A549 cells were maintained in dulbecco's modified eagle medium F12 (DMEM F12) (biological industries) supplemented with 10% fetal bovine serum, 1% penicillin-streptomycin, and 1% L-glutamine (biological industries). All cell lines were incubated at 37°C in a humidified atmosphere containing 5% CO_2 and passaged upon reaching approximately 80% confluence using trypsinization.

Cell viability assay. The cytotoxic effects of the synthesized compounds were assessed using the MTT assay. A549, HeLa, and MCF-7 cells were seeded at a density of 3×10^3 cells/well, PC3 cells at 5×10^3 cells/well, and Caco-2 cells at 8×10^3 cells/well in 96-well plates and allowed to adhere for 24 h [11].

Compounds were dissolved in sterile dimethyl sulfoxide (DMSO) and diluted with culture medium to final concentrations of 1000, 500, 250, 100, 50, and 25 μM, maintaining a final DMSO concentration of 1% in all wells. Treated cells were incubated for 24, 48, and 72 h. At the end of each incubation period, 10 μL of MTT reagent (5 mg/mL in PBS) was added to each well, followed by incubation for 4 h. Cells were then centrifuged at 1800 rpm for 10 min, the supernatant was removed, and formazan crystals were dissolved in DMSO. Absorbance was measured at 540 nm using a Varioskan Flash microplate reader [11].

Apoptosis analysis. The apoptotic effects of the synthesized compounds were evaluated using the FITC Annexin V apoptosis detection kit with propidium iodide (PI) (BioLegend) [12]. Cells (5×10^5/well) were seeded in 6-well plates and incubated for 24 h at 37°C with 5% CO_2. Test compounds were dissolved in sterile DMSO and added at their IC_{50} concentrations. After 48 h of treatment, culture media were collected, and cells were washed with PBS, harvested by trypsinization, and centrifuged at 800 rpm for 5 min. The cell pellet was resuspended in 200 μL of binding buffer, stained with 2 μL Annexin V-FITC and 5 μL PI, and incubated for 15 min in the dark at room temperature. Apoptosis was analyzed using a BD FACSCanto flow cytometer.

Cell cycle analysis. Cells (5×10^5/well) were seeded in 6-well plates and incubated for 24 h at 37°C with 5% CO_2. After 24 h, cells were treated with the IC_{50} concentrations of the test compounds and incubated for an additional 48 h. Following treatment, cells were harvested by trypsinization, washed with cold PBS, and fixed in cold (–20°C) ethanol overnight. Fixed cells were centrifuged at 1200 rpm for 10 min to remove ethanol and PBS, then resuspended in PBS containing 0.1% Triton X-100. RNase A (20 μL, 200 μg/mL) was added, and cells were incubated at 37°C for 30 min. PI (20 μL, 1 mg/mL) was then added, and samples were incubated at room temperature for 15 min. Cell cycle distribution was analyzed using a BD FACSCanto flow cytometer.

Wound healing assay. A scratch assay was performed to study cell migration. Glass coverslips were sterilized with 100% methanol, autoclaved, and placed into 6-well plates. Cells (5×10^5 cells/well) were seeded and incubated for 24 h to allow attachment to the coverslip surface. Upon reaching approximately 90% confluence, a scratch approximately 1 mm wide was created using a sterile 200 μL pipette tip. Non-adherent cells were removed by washing with phosphate-buffered saline (PBS). Test compounds dissolved in DMSO were applied at their IC_{50} concentrations, while untreated cells served as negative controls. Cell migration into the scratch area was observed at 0 and 48 h using an inverted microscope, and images were captured to quantify migration differences.

Molecular docking analysis. Molecular docking studies were conducted to evaluate the binding interactions of synthesized epoxy alcohol derivatives with selected anticancer protein targets [13, 14]. Crystal structures of epidermal growth factor receptor (EGFR, PDB ID: 2ITO, resolution 3.25 Å), c-Met (PDB ID: 4GG5, resolution 2.42 Å), human estrogen receptor alpha (PDB ID: 3ERT, resolution 1.90 Å), androgen receptor (PDB ID: 2AX6, resolution 1.50 Å), and human tankyrase 1 (PDB ID: 4W6E, resolution 1.95 Å) were obtained from the Protein Data Bank (https://www.rcsb.org/).

In silico docking was performed using AutoDock Tools (version 1.5.7) to assess the binding affinity and interactions of epoxy alcohol derivatives relative to known anticancer agents. The compounds' 3D structures were optimized with Avogadro software by converting 2D representations into 3D conformations followed by energy minimization. Target protein structures were prepared by removing water molecules, adding polar hydrogens, and assigning Kollman charges using MGLTools. Ligands' torsion angles were checked and saved in PDBQT format with updated parameters. Docking grids were centered on identified active sites with dimensions of $60 \times 60 \times 60$ Å^3 and grid spacing of 0.553 Å.

The lamarckian genetic algorithm (LGA) was employed to predict protein-ligand binding modes. Non-covalent interactions including hydrogen bonds, van der Waals forces, and polar contacts were analyzed to estimate binding affinities. Docked complexes were visualized and further analyzed using BIOVIA Discovery Studio to interpret interaction profiles. Docking scores and detailed interaction diagrams are presented in Table 2 and Figs. 6 and 9.

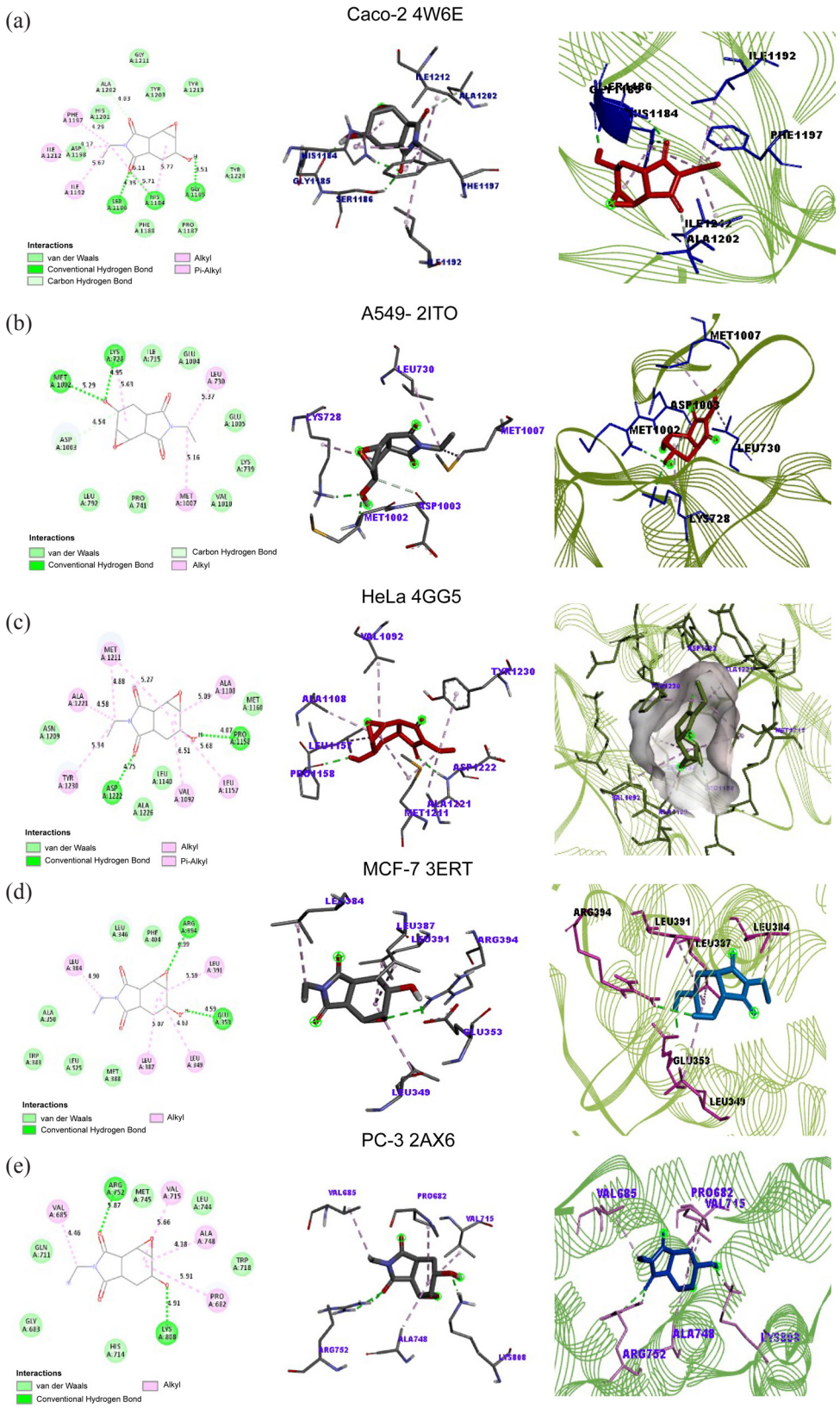

Fig. 9. 3D and 2D representation of binding interactions of (**VIb**) (*N*-Et) with (a) 4W6E, (b) 2ITO, (c) 4GG5, (d) 3ERT, and (e) 2AX6.

ADMET properties. The SwissADME web server (www.swissadme.ch) was utilized to calculate drug-likeness parameters and ADME (absorption, distribution, metabolism, and excretion) profiles for the synthesized compounds [15]. This included key pharmacokinetic parameters, physicochemical properties, and lipophilicity assessments relevant for virtual screening. Specifically, predictions for total polar surface area (TPSA), blood-brain barrier (BBB) permeability, gastrointestinal (GI) absorption, and compliance with Lipinski's rule of five were obtained. SMILES representations for each compound were sourced from PubChem [16].

CONCLUSIONS

In this study, we synthesized four isoindole-1,3-dione derivatives bearing polyoxygenated substituents at the 1,2,3-positions of the cyclohexane ring. The cytotoxic activities of these compounds were evaluated against five different cancer cell lines. Additionally, apoptosis induction and *in vitro* wound healing assays were performed. Compound (**VId**) demonstrated the highest efficacy across all tested cell lines.

The compounds exhibited dose- and time-dependent cytotoxic effects in most cases. Among them, (**VId**) showed significantly higher apoptotic induction after 48 h of treatment compared to other derivatives. *In vitro* wound healing assays on A549 (lung), HeLa (cervical), and PC3 (prostate) cell lines revealed notable inhibition of cell migration, indicating potential antimetastatic properties.

Based on these results, epoxy isoindole derivatives represent promising anticancer agents for the treatment of cervical, lung, prostate, and breast cancers due to their antiproliferative activities. Molecular docking studies further supported these findings, highlighting compound (**VId**) (*N*-benzyl) as a strong candidate with potential therapeutic effects targeting EGFR, TNKS, HGFR (c-Met), human estrogen receptor alpha (hERα), and androgen receptor (AR).

ACKNOWLEDGMENTS

The authors thank Atatürk University and Biotechnology and Bioengineering Center laboratory staff of Izmir Institute of Technology and for the facilities and technical support.

FUNDING

This research was supported by the Tübitak (grant no. 119Z097).

ETHICS APPROVAL AND CONSENT TO PARTICIPATE

This article does not contain any studies involving patients or animals as test objects.

Informed consent was not required for this article.

CONFLICT OF INTEREST

No conflicts of interest was declared by the authors.

AUTHOR CONTRIBUTION

The authors EY, DM, ÖG, and NHK—methodology, ınvestigation, data curation, formal analysis, original draft preparation. The authors GSM and YK—supervision, conceptualization, ınvestigation.

DATA AVAILABILITY

The data that support the findings of this study are available from the corresponding author upon reasonable request.

SUPPLEMENTARY INFORMATION

The online version contains supplementary material available at https://doi.org/10.1134/S1068162024606657

REFERENCES

1. Thebtaranonth, C. and Thebtaranonth, Y., *Acc. Chem. Res.*, 1986, vol. 19, pp. 84–90. https://doi.org/10.1021/ar00123a004
2. Marco-Contelles, J., Molina, M.T., and Anjum, S., *Chem. Rev.*, 2004, vol. 104, pp. 2857–2899. https://doi.org/10.1021/cr980013j
3. Duke, R.K. and Rickards, R.W., *J. Org. Chem.*, 1984, vol. 49, pp. 1898–1904. https://doi.org/10.1021/jo00185a010
4. Gültekin, M.S., Çelik, M., and Balcı, M., *Curr. Org. Chem.*, 2004, vol. 8, pp. 1159–1186. https://doi.org/10.2174/1385272043370069
5. Schulte, G.R., Ganem, B., Chantrapromma, K., Kodpinid, M., and Kobkull, S., *Tetrahedron Lett.*, 1982, vol. 23, pp. 289–292. https://doi.org/10.1016/S0040-4039(00)86811-2

6. Süloğlu, A.K., Selmanoglu, G., Gündoğdu, Ö., Kishalı N.H., Girgin, G., Palabıyık, S., Tan, A., Kara, Y., and Baydar, T., *Arch. Pharm.*, 2020, vol. 353, p. e200006. https://doi.org/10.1002/ardp.202000065
7. Köse, A., Bal, Y., Şanlı Mohamed, G., and Kara, Y., *Med. Chem. Res.*, 2017, vol. 26, pp. 779–786. https://doi.org/10.1007/s00044-017-1793-1
8. Köse, A., Kaya, M., Kishalı, N.H., Akdemir, A., Şahin, E., Kara, Y., and Şanlı-Mohamed, G., *Bioorg. Chem.*, 2020, vol. 94, pp. 103421. https://doi.org/10.1016/j.bioorg.2019.103421
9. Tan, A., Kazancıoğlu, M.Z., Aktaş, D., Gündoğdu, Ö., Şahin, E., Kishalı, N., and Kara, Y., *Turk. J. Chem.*, 2014, vol. 38, pp. 629–637. https://doi.org/10.3906/kim-1310-30
10. Gündoğdu, Ö., Atalay, A., Çelebioğlu, N., Anıl, B., Şahin, E., Şanlı-Mohamed, G., Bozkaya, U., and Kara, Y., *J. Mol. Struct.*, 2022, vol. 1264, p. 133163. https://doi.org/10.1016/j.molstruc.2022.133163
11. Freshney, R.I., Culture of animal cells, *A Manual of Basic Technique*, Freshney, R.I., Ed., Wiley-Liss, New York, 1994, pp. 387–389.
12. Çakmak, Y.Ö., DNA *Fragmantasyonu, Hücre Döngüsünün Analizi ve Apoptotik Hücre Analizi (Annexin-V). Hücre Ölümü Araştırma Teknikleri Teorik Kursu*, 2011, pp. 223–232.
13. Karimov, A., Orujova, A., Taslimi, P., Sadeghian, N., Mammadov, B., Karaman, H.S., Farzaliyev, V., Sujayev, E., Taş, R., Alwasel, S., and Gulcin, I., *Bioorg. Chem.*, 2020, vol. 99, pp. 103762. https://doi.org/10.1016/j.bioorg.2020.103762
14. Mahmudov, I., Demir, Y., Sert, Y., Abdullayev, Y., Saleh, S.A., Alwasel, A., and Gulcin, I., *Arab. J. Chem.*, 2022, vol. 15, pp. 10364. https://doi.org/10.1016/j.arabjc.2022.103849
15. Daina, A., Michielin, O., and Zoete, V., *Sci. Rep.*, 2017, vol. 7, pp. 42717. https://doi.org/10.1038/srep42717
16. Saini, N., Grewal, A.S., Lather, V., and Gahlawat, S.K., *Chem. Biol. Interact.*, 2022, vol. 358, p. 109901. https://doi.org/10.1016/j.cbi.2022.109901
17. Sharma, D.K., Tripathi, A., Sharma, R., Chib, R., Rasool, R., Hussain, A., Singh, B., Goswami, A., Khan, I., and Mukherjee, D., *Med. Chem. Res.*, 2013, vol. 23, pp. 1643–1653. https://doi.org/10.1007/S00044-013-0764-4
18. Meng, X.Y., Zhang, H.X., Mezei, M., and Cui, M., *Curr. Comput. Aided Drug Des.*, 2011, vol. 7, pp. 146–157. https://doi.org/10.2174/157340911795677602
19. Sarı, S., *Hacet. Univ. J. Fac. Pharm.*, 2020, vol. 40, pp. 34–47.
20. Zhuang, C., Zhang, W., Sheng, C., Zhang, W., Xing, C., and Miao, Z., *Chem. Rev.*, 2017, vol. 117, pp. 7762–7810. https://doi.org/10.1021/acs.chemrev.7b00020
21. Lunardi, F., Guzela, M., Rodrigues, A.T., Corrêa, R., Eger-Mangrich, I., Steindel, M., Grisard, E.C., Assreuy, J., Calixto, J.B., and Santos, A.R.S., *Antimicrob. Agents Chemother.*, 2003, vol. 47, p. 1449. https://doi.org/10.1128/aac.47.4.1449-1451.2003
22. Bijani, S., Iqbal, D., Mirza, S., Jain, V., Jahan, S., Alsaweed, M., Madkhali, Y., Alsagaby, S.A., Banawas, S., and Algarni, A., *Life*, 2022, vol. 12, p. 519. https://doi.org/10.3390/life12040519
23. Lehtiö, L., Chi, N.W., and Krauss, S., *FEBS J.*, 2013, vol. 280, pp. 3576–3593. https://doi.org/10.1111/febs.12320
24. Neagu, G., Stefaniu, A., Albulescu, A., Pintilie, L., and Pirvu, L.C., *Appl. Sci.*, 2021, vol. 11, pp. 9944. https://doi.org/10.3390/app11219944
25. Kim, B., Jung, N., Lee, S., Sohng, J.K., and Jung, H.J., *Phytother. Res.*, 2016, vol. 30, pp. 1833–1840. https://doi.org/10.1002/ptr.5689
26. Wang, L., Wu, R., Fu, W., Lao, Y., Zheng, C., Tan, H., and Xu, H., *Bioorg. Med. Chem.*, 2016, vol. 24, pp. 4120–4128. https://doi.org/10.1016/j.bmc.2016.06.054
27. Venkatesham, P., Shyam, P., Chedupaka, P.R., Pooja, R., and Vedula, R.R., *Aromat. Comp.*, 2023, vol. 43, p. 2283. https://doi.org/10.1080/10406638.2022.2042333(28)
28. Ashtekar, S.S. and Bhatia, N.M., *J. Mol. Struct.*, 2022, vol. 1268, pp. 133687. https://doi.org/10.1016/j.molstruc.2022.133687

29. Chaitanya, V.K., Jalapathi, P., Chandar, M.R., Vishnu, T., Veerabhadraiah, M., and Raghavender, M., *Iran. Chem. Soc.*, 2023, vol. 20, pp. 995–1006. https://doi.org/10.1007/s13738-022-02737-y
30. Rezaei-Seresht, H., Cheshomi, H., Falanji, F., Movahedi-Motlagh, F., Hashemian, M., and Mireskandari, E., *Avicenna J. Phytomed.*, 2019, vol. 9, pp. 574–586. https://doi.org/10.22038/AJP.2019.13475
31. Tan, M.H., Li, J., Xu, H.E., Melcher, K., and Yong, E.L., *Acta Pharmacol. Sin.*, 2015, vol. 36, pp. 3–23. https://doi.org/10.1038/aps.2014.18
32. Lotfy, K., *Biophys. Chem.*, 2015, vol. 6, pp. 91–117. https://doi.org/10.4236/jbpc.2015.64010
33. Radaeva, M., Li, H., LeBlanc, E., Dalal, K., Ban, F., Ciesielski, F., Chow, B., Morin, H., Awrey, S., Singh, K., Rennie, P.S., Lallouz, N., and Cherkasov, A., *Cells*, 2022, vol. 11, pp. 2785. https://doi.org/10.3390/cells11182785
34. Tatar, R.G. and Kurşun Aktar, B.S., *Int. J. Adv. Eng. Pure Sci.*, 2021, vol. 33, pp. 660. https://doi.org/10.7240/jeps.945430

AI tools may have been used in the translation or editing of this article.